Inference of proto-neutron star properties from gravitational wave data in core-collapse supernovae.

I. INTRODUCTION

The life of massive stars (those born with masses between ~ 8 M$_\odot$ and ~ 120 M$_\odot$) ends with the collapse of the iron core under its own gravity, leading to the formation of a neutron star (NS) or a black hole (BH), and followed (typically but not necessarily in the BH case) by a supernova explosion. Nearby core-collapse supernova (CCSN) explosions are expected to be sources of gravitational waves (GWs) and are one of the main candidates for the next great discovery by current ground-based observatories. However, these are relative rare events. A neutrino-driven explosion [1] is the most likely outcome in the case of slow rotating cores, which are present in the bulk of CCSN progenitors. The emitted GWs could be detected with advanced ground-based GW detectors (Advanced LIGO[2], Advanced Virgo[3] and KAGRA[4]) within 5 kpc [5, 6]. Such a galactic event has a rate of about $2-3$ per century [7, 8]. For the case of fast rotating progenitor cores the result is likely a magneto-rotational explosion, with a more powerful GW signal that could be detected within 50 kpc and for some extreme models up to $5-30$ Mpc [5, 6]. However, only about 1% of the electromagnetically observed events show signatures of fast rotation (broad-lined type Ic SNe [9] or events associated to long GRBs [10]), making this possibility a subdominant channel of detection with an event rate of $\sim 10^{-4}$yr^{-1}add ref?. Therefore, we focus this work only in neutrino-driven CCSNe. Despite the low rates, CCSN are of great scientific interest because they produce a complex GW signals which could provide significant clues about the physical processes that occur in the moments after the collapse.

In the last decade, significant progress has been made in the development of numerical codes, in particular in the treatment of multidimensioal effects [11]. In the case of neutrino-driven explosions, the GW emission is primarly induced by instabilities developed at the newly formed proto-neutron star (PNS) and by the non-spherical accreting flow of hot matter over its surface [12]. This dynamics excite the different modes of oscillation of the PNS, which ultimately leads to the emission of GWs. The frequency and time evolution of these modes carry information about the properties of the GW emitter and could allow to perform PNS asteroseismology.

The main feature appearing systematically in the GW spectrum of multidimensional numerical simulations is a strong and relatively narrow oscillation in the post bounce evolution with raising frequency from about 100 Hz up to a few kHz (at most) and a typical duration of $0.5-1$ s. This feature has been interpreted as a continuously excited gravity mode (g-mode, see [13, 14] for a definition in this context) of the PNS [15–20]. In these models the monotonic raise of the frequency of the mode is related to the contraction of the PNS. The typical frequencies of these modes make them a promising source for ground-based interferometers.

The properties of g-modes in hot PNSs have been studied since the end of last century by means of linear perturbation analysis of background PNS models. The oscillation modes associated to the surface of hot PNSs was first considered by McDermott, van Horn & Scholl [21]. Additionally, the stratified structure of the PNS allows the presence of different types of g-modes related with the fluid core [22]. Many posterior works used simplified neutron star models assuming an equilibrium configuration as a background, to study the effect of rotation [23], general relativity [24], non-linearities [25], phase transition [26] and realistic equation of state [27]. Only recently, there has been an effort to incorporate realistic backgrounds based in numerical simulations in the computation of the mode structure and evolution [28–36].

The eigenmode spectrum of the region within the shock (including the PNS and the post-shock region) using results from 2D CCSN numerical simulations as a background studied in [29, 31] show a good match of the mode frequencies computed and the features observed in the GW spectrum of the same simulation (specially when space-time perturbations are included [31]). This result reveals that it is posible to perform CCSN asteroseismology under realistic conditions and serves as a starting point to carry out inference of astrophysical parameters of PNSs. [32] went one step further showing that it was possible to derive simple relations between the instantaneous frequency of the g-mode and the mass and radius of the PNS at each time of the evolution. These relations are universal in the sense that they do not depend on the equation of state (EOS) used or the mass of the progenitor, and only weakly on the numerical code used (see discussion in section II). Similar relations have been found by [35, 36], which also found that the universal relations do not depend on the dimensionality (1D, 2D or 3D) of the numerical simulation used as a background.

In this work, we present a method to infer from the GW data alone, the time evolution of some properties or the PNS, namely a combination of its mass and radius. For this purpose we have developed an algorithm to extract the time-frequency evolution of the main feature in the spectrograms of the GW emission of 2D simulations of CCSN. This feature corresponds to the $^2g_2$ mode, according to the nomenclature used in [32] (different authors may have slightly different naming convention). Next, we use the universal relations obtained by [32], based on a set of 1D simulations, to infer the time evolution of the ratio $M_{\rm PNS}/R_{\rm PNS}^2$, being $M_{\rm PNS}$ and $R_{\rm PNS}$ the mass and radius of the PNS. Using 2D CCSN waveform corre-

sponding to different progenitor masses we estimate the performance of the algorithm for current and future generation of ground-based GW detectors.

This paper is organised as follows. Section II describes the details of the CCSN simulations used in the paper. Section III focuses on the algorithm that extracts the time evolution of a combination of the mass and radius of the PNS corresponding to a g-mode. Section IV shows the performance of the data analysis method with simulated GW detectors data. Finally, we discuss the results in section V.

II. CORE COLLAPSE SUPERNOVA SIMULATIONS

Unless other methods used GW astronomy, the algorithm proposed in this work does not require accurate waveforms in order to infer the properties of the PNS. Instead, it relies on the evolution of the frequency of oscillation of some particular modes, as seen in the GW spectrum. The frequency of these modes depends, in a universal way, on the surface gravity of the PNS $(r = M_{\mathrm{PNS}}/R_{\mathrm{PNS}}^2)$, in the sense that if at a given time we observe GW emission at a certain frequency f we can determine univocally the value of the surface gravity, within a certain error, regardless of the details of the numerical simulation. In this work we use two sets of simulations: i) The *model set*, composed by 1D simulations, which is used to build the universal relation (model), $r(f)$, linking the ratio r with the observed frequency f, and ii) the *test set*, composed by 2D simulations, for which we know both the GW signal and the evolution of the ratio, $r(t)$, and that is used to test performance of the algorithm.

We have used two different numerical codes in our numerical simulations. CoCoNuT [37, 38] is a code for general relativistic hydrodynamics coupled to the Fast Multigroup Transport scheme [39] providing an approximate description of the emission and transport of neutrinos. AENUS-ALCAR [40] combines special relativistic (magneto-)hydrodynamics, a modified Newtonian gravitational potential approximating the effects of general relativity [41], and a spectral two-moment neutrino transport solver [40]. We included the relevant reactions between matter and neutrinos of all flavours, i.e., emission and absorption by nucleons and nuclei, electron-positron pair annihilation, nucleonic bremsstrahlung, and scattering off nucleons, nuclei, and electrons.

For the *model set*, we use the 25 spherically symmetric (1D) simulations of [31] including progenitors with zero-age main sequence (ZAMS) masses in the range $M_{\mathrm{ZAMS}} = 11.2 - 75\,M_\odot$. The set contains simulations using the two numerical codes and six different equations of state. Details can be found in [31]. The reason to use one dimensional simulations for the model set is that the computational cost of those is significantly smaller than the cost of multidimensional simulations, so is easier to

Model name	M_{ZAMS} [$M_\odot$]	progenitor model	EOS	t_{f} [s]	$t_{\mathrm{explosion}}$	$M_{\mathrm{PNS,f}}$ [$M_\odot$]
s11	11.2	[42]	LS220	1.86	$\times$	1.47
s15	15.0	[42]	LS220	1.66	$\times$	2.00
s15S	15.0	[42]	SFHo	1.75	$\times$	2.02
s15G	15.0	[42]	GShen	0.97	$\times$	1.86
s20	20.0	[42]	LS220	1.53	$\times$	1.75
s20S	20.0	[43]	SFHo	0.87	$\times$	2.05
s25	25.0	[42]	LS220	1.60	0.91	2.33
s40	40.0	[42]	LS220	1.70	1.52	2.23

TABLE I. List of axisymmetric simulations used for the *test set*. The last three columns show, the post-bounce time at the end of the simulation, the one at the onset of the explosion (non exploding models marked with $\times$), and the PNS mass at the end of the simulation.

accumulate the statistics necessary to build a good model for $r(f)$. For each time of each simulation we compute the ratio r and the frequency of the $^2g_2$ mode by means of the linear analysis described in [29, 31, 32].

For the *test set*, we use 8 axisymmetric (2D) simulations using the AENUS-ALCAR code (see Table I for a list of models). 7 of these simulations use a selection of progenitors with masses in the range $M_{\mathrm{ZAMS}} = 11.2 - 40\,M_\odot$ evolved through the hydrostatic phases by [42]. We performed one simulation of each stellar model using the equation of state of [44] with an incompressibility of $K = 220\,\mathrm{MeV}$ (LS220) and added comparison simulations with the SFHo EOS [45] and the GShen EOS [46] for the progenitor with $M_{\mathrm{ZAMS}} = 15\,M_\odot$. To this set of simulations, we add the waveform of a two-dimensional model used in [31], denoted s20S. It corresponds to a star with the same initial mass, $M_{\mathrm{ZAMS}} = 20\,M_\odot$, as for one of the other 7 axisymmetric simulations, but was taken from a newer set of stellar-evolution models [43]. It was evolved with the SFHo EOS.

For all the simulations, we mapped the pre-collapse state of the stars to a spherical coordinate system with $n_r = 400$ zones in radial direction distributed logarithmically with a minimum grid width of $(\Delta r)_{\mathrm{min}} = 400\,\mathrm{m}$ and an outer radius of $r_{\mathrm{max}} = 8.3 \times 10^9\,\mathrm{cm}$ and $n_\theta = 128$ equidistant cells in angular direction. For the neutrino energies, we used a logarithmic grid with $n_e = 10$ bins up to 240 MeV. Unlike the model set, the simulations in the test set are not 1D because we need to extract the gravitational wave signal, which is a multi-dimensional effect. For each simulation we extract the gravitational wave signal, $h_+(t)$, by means of the quadrupole formula and compute the time evolution of the surface gravity, $r(t)$.

All spherical and most axisymmetric models fail to achieve shock revival during the time of our simulations. Only the two stars with the highest masses, s25 and s40, develop relatively late explosions in axisymmetry. Consequently, mass accretion onto the PNSs proceeds at high rates for a long time in all cases and

causes them to oscillate with their characteristic frequencies. The final masses of the PNSs are in the range of $M_{\mathrm{PNS}} = 1.47 - 2.33\,M_\odot$, i.e., insufficient for producing a black hole.

III. METHODS DESCRIPTION

In this section, we outline a strategy for estimating the time evolution of the ratio $r = M_{\mathrm{PNS}}/R_{\mathrm{PNS}}^2$ of the mass of the PNS and its squared radius (in units of solar mass and km) from the observation of the $^2g_2$ oscillation mode in the gravitational wave detector data. An integral part of this strategy is the universal relations that relate the characteristic frequency of the PNS oscillation f, g and p modes with the mass and the radius of the PNS, the shock radius and the total mass inside the shock as demonstrated in [32].

To build the model of the ratio r as a function of the frequency f we use the spherically symetric (1D) simulations of the *model set*. Figure 1 shows the data for the 25 numerical simulations. As identified by [32], the only systematic deviation from a single universal relation is the numerical code used in the simulations. To avoid any systematic effect, we only use the 18 simulations performed with the ALCAR-AENUS code, which is the same code that was used in our test set. The consequences of this choice are discussed in the conclusions. Using this data, we parametrize the ratio with a cubic polynomial regression with heteroscedastic errors

$$r_i = \beta_1 f_i + \beta_2 f_i^2 + \beta_3 f_i^3 + \epsilon_i \tag{1}$$

where ϵ_i are assumed to be independent zero-mean Gaussian errors with variances σ_i^2 that increase with frequency f_i. The model for frequency-dependent variances is

$$\log \sigma_i = \alpha_0 + \alpha_1 f_i + \alpha_2 f_i^2 + \delta_i \tag{2}$$

with independent and identically zero-mean Gaussian errors δ_i. The R-package `lmvar` [47] that implements a maximum likelihood approach was used to fit the model.

The best fitting model amongst polynomials of degree 1, 2, and 3 was chosen according to the Aikaike information criterion with coefficients given in Table II, which is actually the model defined in (1). The data and fit of the model including 95% confidence bands are displayed in Figure 1.

We use this model to infer the properties of the simulations in the *test set* described in in Section II. To describe the method we focus on the gravitational wave signal of `s20S`, originally sampled at 16384 Hz but resampled at 4096 Hz. A spectrogram of this signal is shown in Figure 2 based on autoregressive estimates [CITATION?] of the local spectra for successive time intervals of length 200 with a 90% overlap. The dominant emission mode corresponds to the PNS oscillation $^2g_2$-mode. We have

Coefficient	Estimate	Standard error
β_1	1.00×10^{-06}	2.12×10^{-08}
β_2	-8.22×10^{-10}	5.00×10^{-11}
β_3	1.01×10^{-12}	2.70×10^{-14}
α_0	$-1.02 \times 10^{+01}$	6.80×10^{-02}
α_1	7.24×10^{-04}	1.56×10^{-04}
α_2	6.23×10^{-07}	8.15×10^{-08}

TABLE II. Estimate and standard error of the coefficients of the best fit model describing the ratio $r = M_{\mathrm{PNS}}/R_{\mathrm{PNS}}^2$ as function of the frequency of the $^2g_2$ mode.
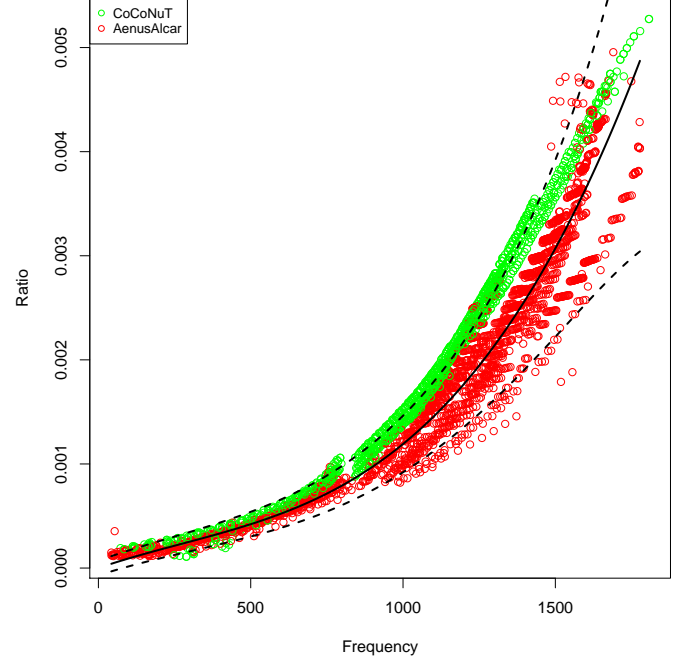

FIG. 1. Ratio $M_{\mathrm{PNS}}/R_{\mathrm{PNS}}^2$ from 25 1D simulations AENUS-ALCAR (red) and CoCoNuT (green) code. The solid line is the maximum likelihood estimate of heteroscedastic cubic model with 95% confidence bands (dashed lines) considering only the AENUS-ALCAR data points (18 simulations).

developed a time-frequency method to track the ridge $m(t)$ in the spectrogram, taking into account that it is monotonically increasing as time goes. This is a property of the $^2g_2$-mode, the frequency of which increases as the object becomes more massive and compact. Starting from either the left- or right-most column of the time-frequency matrix we identify and trace the sequence of amplitude peaks within a certain frequency band given the monotonicity constraint. Appendix A is providing more details on the reconstruction of the g mode ridge.

We collect the instantaneous frequency $f(t_i)$ corresponding to the ridge $m(t_i)$ for the midpoint t_i of each local time interval of the spectrogram and interpolating $f(t)$ for values in between the t_i. We then use our model given by Eq. (1) to obtain estimates of the time evolution of the ratio together with 95% confidence intervals.
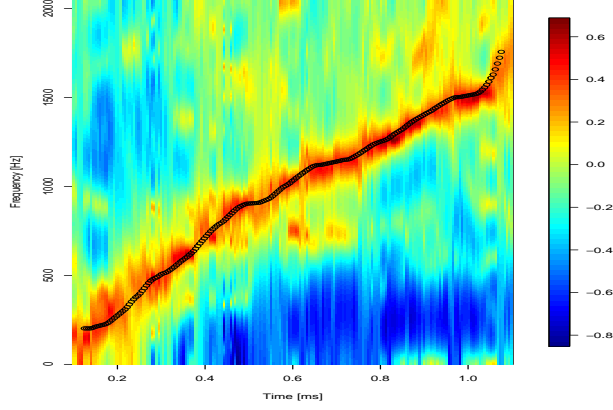
FIG. 2. Spectrogram of the gravitational wave signal s20S sampled at 4096 Hz. The spectrogram is obtained using data streach of 200 samples overlapping at 90% with each other.
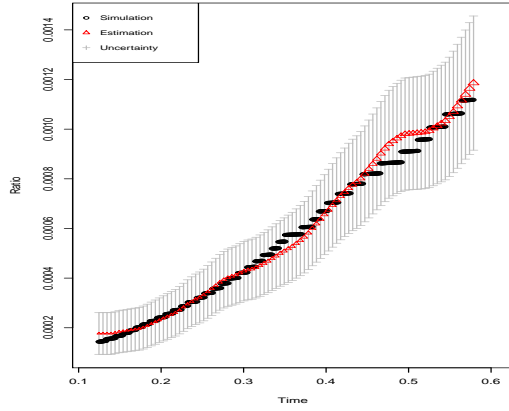

FIG. 3. Ratio M_{PNS}/R_{PNS}^2 as function of time extracted from the $^2g_2$-mode of the s20S signal (red points and the 95% confidence belt in grey) compared to the ratio value derived from the PNS mass and radius given by the simulation code (black points) To be redone in python.

An exemple is given in Figure 3 where the red points are the point estimates and the grey bands represent 95% confidence bands. Ratio values computed using the mass and radius values obtained from the simulation code (true values) are shown in black.

In this case, for a GW signal without any noise, the coverage of our 95% confidence band is 100% of the true values. In the next section we investigate the performance of the reconstruction of $r(t)$ when the gravitational wave signal is embedded in noise.
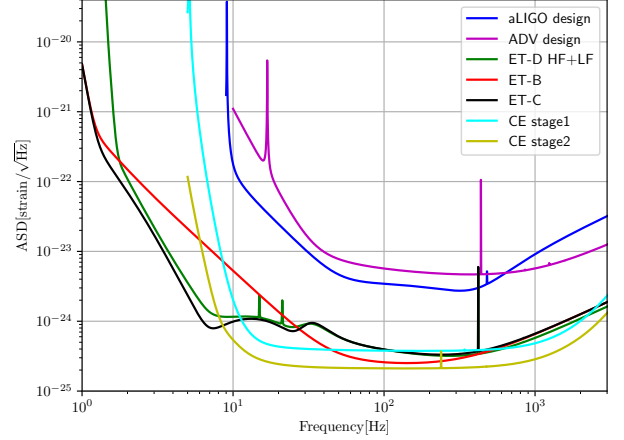

FIG. 4. Amplitude spectral density of the GW detectors advanced LIGO (aLIGO) and Advanced Virgo (ADV) at design sensitivity and of the proposed third generation detectors Cosmic Explorer and Einstein Telescope. Eintein Telescope sensitivity curve ET-B is obtained pushing second generation detector technology at its limit. ET-C and ET-D sensitivity curves correspond to a detector configuration where a low-power cryogenic low-frequency interferometer and a high-power room temperature high-frequency interferometer are sharing the same infrastructure [?]. Cosmic Explorer design sensitivity will be achieved in two stages. Stage 1 (CE1) is expected to use the technology developed for the "A+" upgrade to advanced LIGO but scaled up to a 40 km detector while stage 2 (CE2) will implement state-of-the-art technology to decrease quantum and thermal noises [49].

IV. DETECTION SENSITIVITY WITH ADVANCED GRAVITATIONAL WAVE DETECTORS

To estimate how accurately we can infer the time evolution of $r = M_{PNS}/R_{PNS}^2$ in the gravitational wave detector data, we have added the GW signal from s20S to 100 Gaussian noise realisations whose power spectral density follows the advanced LIGO (aLIGO) spectrum [48] shown on Figure 4.

We have varied the distance to the source, covering a large range of distances for which a detection in second generation of gravitational wave detectors is feasible. The source is optimally oriented with respect to the gravitational wave detector. We are assuming a GW signal from a core collapse phenomena has been identified in the data and that the beginning of the GW signal is known within $O(10~ms)$. The data (signal embedded in noise) are whitened using the function *prewhiten* of the R-package TSA. An auto-regressive model with maximal 100 coefficients has been used.

For each of the noise realisations, we reconstruct the ratio time series r_i of length N starting from the left side of the spectrogram and constraining the beginning of the track to be smaller than 200 Hz. The reconstructed ratio

is then compare to the "true" ratio r_i^0 derived from the PNS mass and radius computed from the s20S simulation.

Figure 5 is showing the distribution of the fraction of the ratio r_i^0 values that fall within the 95% confidence interval of r_i. This quantity, *coverage*, is taking maximal values when the source is located within few kpc and then decreases with the distance.

To better quantify how well we reconstruct the ratio, we have also considered Δ the mean over the track of the relative error of r_i.

$$\Delta = \frac{1}{N} \sum_1^N \frac{|r_i - r_i^0|}{r_i^0} \qquad (3)$$

Δ values of each of the 100 noise realisation are shown as well as function of the distance on Figure 5. For a source located up to ~ 9 kpc the relative error remains smaller than 20%. At small distance, Δ is small but not null. This reflects the approximation of the model used for r. It is nevertheless remarkable that, on average, one can reconstruct the ratio time series with a good precision at distance up to ~ 9 kpc for this particular waveform, with *coverage* value larger than 80%. There are few noise realisations for a source located at < 9 kpc for which Δ takes large values, indicating that the method start failing to reconstruct with accuracy the ratio.

We have tested that the method does not depend on features of s20S using the 7 other waveforms of the *test set* described in section II covering a large range of progenitor masses.

Figure 6 shows that apart s11.2-LS220 and to a lesser extent s20.0-SFHo, the ratio is well reconstructed for all waveforms up to $\sim$ 15kpc. In an effort to better determine the maximal distance of the source at which we can reconstruct the ratio we have run 100 simulations without injecting a signal and have measured *coverage* for the reconstructed ratios. The median of *coverage* as well as the 95 quartile are shown on Figure 6. The noise only median value is null in this case, but it can be different from zero because the g-mode reconstruction algorithm is looking for a continuously frequency increasing track in the spectrogram, starting between 0 and 200 Hz, where we expect the GW signal to be. This is enhancing the probability of overlap. This effects explains why outliers can reach values as high as 80%. Figure 7 shows Δ as function of the distance for the same signals as well as the result when only noise is considered. In Table III we are reporting the distance d_r at which *coverage* median is lower than 95% of the noise only values. We have checked that *coverage* and Δ provide similar values. These numbers are an estimate of the order of magnitude of the source maximal distance at which a reconstruction of the ratio could be possible with current GW detectors. They are also upper limits as we are taking into account the detector antenna response in our simulation but consider the source is optimally oriented. Table III reports also
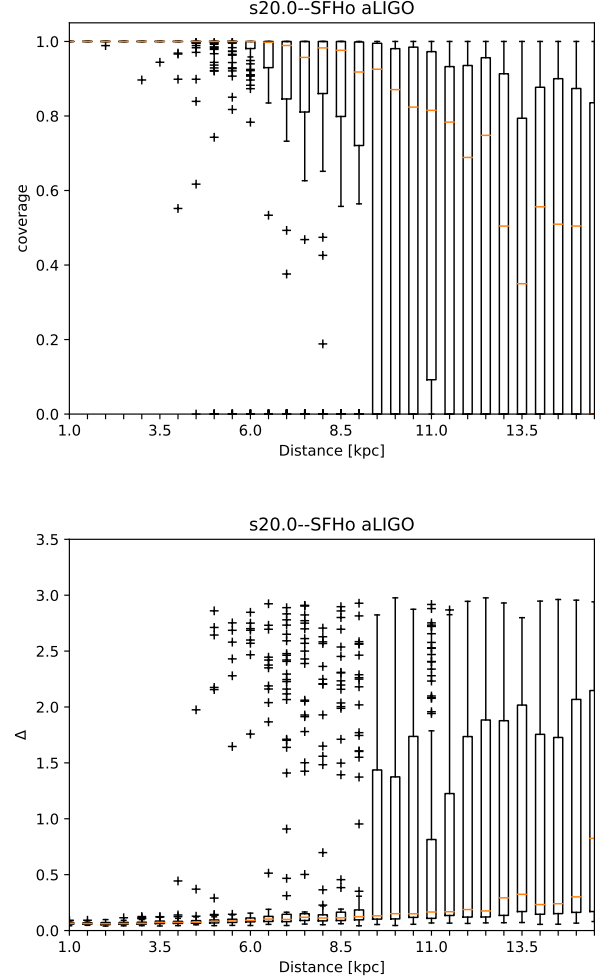

FIG. 5. Boxplots of *coverage* (upper panel) and Δ (lower panel) for s20S signal embedded in aLIGO noise at different distances from the Earth. 100 noise realisations is considered for each distance.

d_r for the advanced Virgo detector at design sensitivity. Results are very similar to aLIGO, despite the detector sensitivity differences. Note that Table III provides the distance at which one could detect a source optimally oriented with a matched filter signal-to-noise ratio of 13.

The same analysis has been performed using expected sensitivity curves for the third generation of gravitational wave detectors. In Europe the Einstein Telescope project proposes to host in a 10-km equilateral triangle configuration 3 low-power low-frequency cryogenic interferometers as well as 3 high-power high-frequency interferometers. Three sensitivity curves, ET-B, ET-C and ET-D corresponding to different options and stages of the project [50] are considered in this study. The US based project Cosmic Explorer [49] is proposing to reach its design sensitivity circa 2040 through two phases labeled CE1 and CE2 also shown in Figure 4.

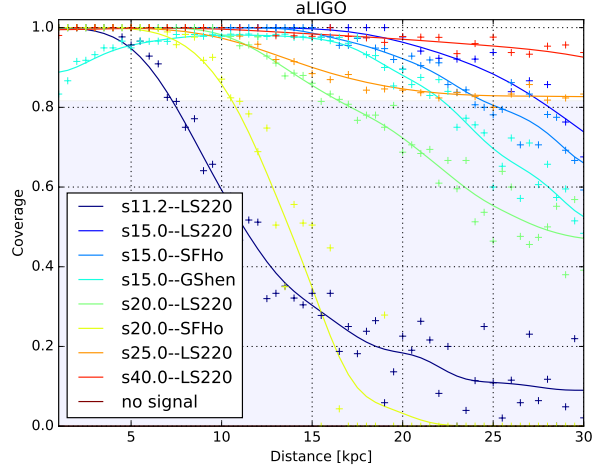Figure 8 shows Δ as function of the source distance

FIG. 6. Median of *coverage* for 8 CCSN waveforms embedded in aLIGO noise and located at different distance from the Earth. The "no signal" line and band show the median and first and third quartile of *coverage* in absence of any signal.
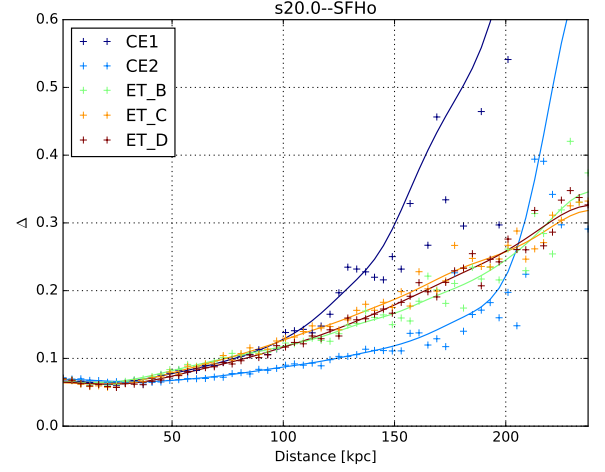

FIG. 8. Median of Δ for s20.0–SFHo CCSN waveform embedded in 3G detectors noise and located at different distance from the Earth.
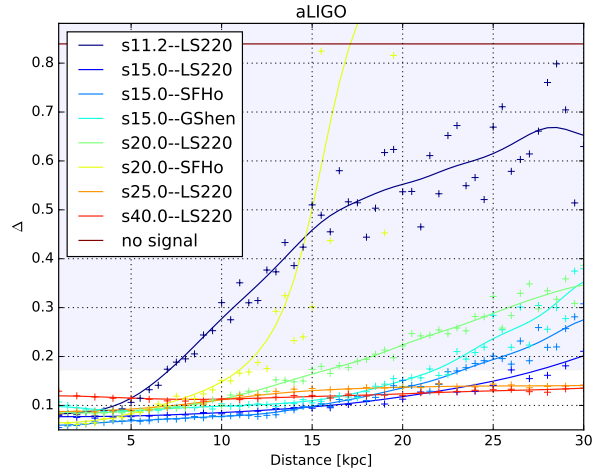

FIG. 7. Median of *Delta* for 8 CCSN waveforms embedded in aLIGO noise and located at different distance from the Earth. The "no signal" line and band show the median and first and third quartile of *Delta* in absence of any signal.
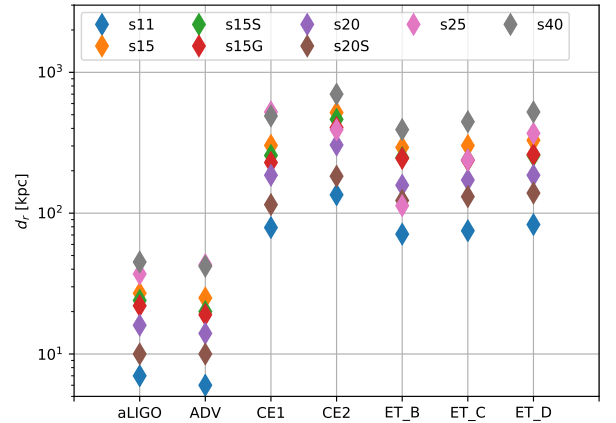

FIG. 9. Maximal distance d_r at which the ratio $r = M_{\mathrm{PNS}}/R_{\mathrm{PNS}}^2$ is reconstructed with good accuracy for a source optimally oriented with respect to the GW detectors for the 7 CCSN waveforms considered in this study.

for s20.0-SFHo waveform for the 5 3G detectors configurations. Overall, the ratio is well reconstructed up to distances in the range 100–200[kpc] which represents an improved of at least a factor 10 with respect to advanced LIGO and advanced Virgo detectors. We can also note that the Einstein Telescope results lay in between the 2 Cosmic Explorer results. This is confirmed for all other waveforms, expect s25.0-LS220 for which the maximal distance reach in CE2 is significantly lower than CE1. This is partly due to the small variation of the reconstruction quality to the distance of the source making the estimation of d_r rather incertain for this waveform.

All results are summarized in Table III and Figure 9. It is remarkable that with 3G detectors the ratio could be reconstructed for sources located up to several hundred of kpc. It is nevertheless important to note the rather large range obtained for the different waveforms probing a large range of progenitor masses.

add comment on the mass progenitor dependence
say that the main depend is the SNR as shown by ddet

		s11	s15	s15S	s15G	s20	s20S	s25	s40
aLIGO	d_r	7	28	24	22	16	11	38	46
	d_{det}	11	36	26	27	21	16	74	61
ADV	d_r	7	26	20	19	15	10	43	42
	d_{det}	10	32	22	23	18	13	64	52
CE1	d_r	79	304	258	229	187	115	524	490
	d_{det}	115	377	270	282	217	168	774	633
CE2	d_r	135	499	451	405	305	183	391	898
	d_{det}	197	649	468	489	375	294	1347	1100
ET_B	d_r	71	293	248	245	158	123	113	392
	d_{det}	106	364	274	391	216	200	805	665
ET_C	d_r	75	302	239	237	172	131	239	446
	d_{det}	97	332	246	260	194	164	727	603
ET_D	d_r	83	329	257	261	186	139	369	523
	d_{det}	107	368	271	285	213	174	796	661

TABLE III. Maximal distance d_r at which the ratio $r = M_{\mathrm{PNS}}/R_{\mathrm{PNS}}^2$ is reconstructed with good accuracy for a source optimally oreinted with respect to the GW detectors considered in this study. d_{det} is the distance at which one could detect a source optimally oriented with a matched filter signal-to-noise ratio of 13 in the different GW detectors.

V. DISCUSSION

Acknowledgments —

Appendix A G-MODE RECONSTRUCTION

Given the spectrogram and an specified time interval for the g-mode reconstruction, our proposal method works as follows. The starting point must be specified. It can be either at the beginning or at the end of the signal. Then, in one of these extremes, the maximum energy value is identified, registering its frequency. This is done independently for a number of consecutive time intervals. Then we calculate the median of these frequency values, providing a robust starting value for the g-mode reconstruction.

The starting frequency value is the first g-mode estimate for the first or the last time interval, depending on the specified starting location. If the reconstruction is set to start at the beginning of the signal, the reconstruction will be done progressively over the time intervals, where each maximum frequency value will be calculated within a frequency range specified by the previous g-mode estimate. Given the non-decreasing behaviour of the true g-mode values, the g-mode estimates will be forced to be greater or equal than the one estimated for its previous time interval, and lower than a specified upper limit. As a result, the g-modes estimates will be a non-decreasing sequence of frequency values.

If the reconstruction is set to start at the end of the signal, the g-modes will be estimated backward in time. Each maximum frequency is calculated within a range determined by its successor (in time) g-mode estimate. These estimates are forced to be lower or equal than its successor (in time) estimate, but greater than a specified lower limit. Thus, a non-decreasing sequence of g-mode estimates is guaranteed.

This g-mode reconstruction method works if and only if the signal is strong enough to provide information about the g-mode, which is reflected in the spectrogram.

Given the sequence of g-mode estimates, the confidence band will be calculated by using the model defined in (1). The g-mode estimates are frequency values which we use as predictors in the model in order to generate confidence intervals for the ratios. Since the g-mode estimates are indexed by time, the confidence intervals for the ratios are too. Thus, we generate the confidence band by interpolating the lower and upper limits of the collection of consecutive confidence intervals, which will be valid for the time range of the g-mode estimates. This confidence band is used to estimate the coverage probabilities in our simulation studies presented ~~below~~ above.

[1] H. A. Bethe, "Supernova mechanisms," Rev. Mod. Phys. **62**, 801–866 (1990).

[2] J. Aasi et al. (LIGO Scientific), "Advanced LIGO," Class. Quant. Grav. **32**, 074001 (2015), arXiv:1411.4547 [gr-qc].

[3] F. Acernese et al. (VIRGO), "Advanced Virgo: a second-generation interferometric gravitational wave detector," Class. Quant. Grav. **32**, 024001 (2015), arXiv:1408.3978 [gr-qc].

[4] Y. Aso, Y. Michimura, K. Somiya, M. Ando, O. Miyakawa, T. Sekiguchi, D. Tatsumi, and H. Yamamoto (KAGRA), "Interferometer design of the KAGRA gravitational wave detector," Phys. Rev. **D88**, 043007 (2013), arXiv:1306.6747 [gr-qc].

[5] S.E. Gossan, P. Sutton, A. Stuver, M. Zanolin, K. Gill, and C. Ott, "Observing gravitational waves from core-collapse supernovae in the advanced detector era," Physical Review D **93** (2016), 10.1103/physrevd.93.042002.

[6] B. P. Abbott and et al, "Optically targeted search for gravitational waves emitted by core-collapse supernovae during the first and second observing runs of advanced LIGO and advanced Virgo," Phys. Rev. D **101**, 084002 (2020), arXiv:1908.03584 [astro-ph.HE].

[7] Scott M. Adams, C. S. Kochanek, John F. Beacom, Mark R. Vagins, and K. Z. Stanek, "Observing the Next Galactic Supernova," ApJ **778**, 164 (2013), arXiv:1306.0559 [astro-ph.HE].

[8] Karolina Rozwadowska, Francesco Vissani, and Enrico Cappellaro, "On the rate of core collapse supernovae in the milky way," New A **83**, 101498 (2021), arXiv:2009.03438 [astro-ph.HE].

[9] Weidong Li, Jesse Leaman, Ryan Chornock, Alexei V. Filippenko, Dovi Poznanski, Mohan Ganeshalingam, Xiaofeng Wang, Maryam Modjaz, Saurabh Jha, Ryan J. Foley, and Nathan Smith, "Nearby supernova rates from the Lick Observatory Supernova Search - II. The observed luminosity functions and fractions of supernovae in a complete sample," MNRAS **412**, 1441–1472 (2011), arXiv:1006.4612 [astro-ph.SR].

[10] Robert Chapman, Nial R. Tanvir, Robert S. Priddey, and Andrew J. Levan, "How common are long gamma-ray bursts in the local Universe?" MNRAS **382**, L21–L25 (2007), arXiv:0708.2106 [astro-ph].

[11] Bernhard Müller, "Hydrodynamics of core-collapse supernovae and their progenitors," Living Reviews in Computational Astrophysics **6**, 3 (2020), arXiv:2006.05083 [astro-ph.SR].

[12] Kei Kotake and Takami Kuroda, "Gravitational Waves from Core-Collapse Supernovae," in Handbook of Supernovae, edited by Athem W. Alsabti and Paul Murdin (2017) p. 1671.

[13] K.D. Kokkotas and B.G. Schmidt, "Quasi-normal modes of stars and black holes," Living Rev. Rel. **2**, 2 (1999).

[14] John L. Friedman and Nikolaos Stergioulas, Rotating Relativistic Stars (2013).

[15] J. W. Murphy, C. D. Ott, and A. Burrows, "A Model for Gravitational Wave Emission from Neutrino-Driven Core-Collapse Supernovae," ApJ **707**, 1173 (2009).

[16] B. Müller, H.-T. Janka, and A. Marek, "A New Multi-dimensional General Relativistic Neutrino Hydrodynamics Code of Core-collapse Supernovae. III. Gravitational Wave Signals from Supernova Explosion Models," ApJ **766**, 43 (2013), arXiv:1210.6984 [astro-ph.SR].

[17] Pablo Cerdá-Durán, Nicolas DeBrye, Miguel A. Aloy, José A. Font, and Martin Obergaulinger, "Gravitational Wave Signatures in Black Hole Forming Core Collapse," Astrophys. J. Lett. **779**, L18 (2013), arXiv:1310.8290 [astro-ph.SR].

[18] Konstantin N. Yakunin, Anthony Mezzacappa, Pedro Marronetti, Shin'ichirou Yoshida, Stephen W. Bruenn, W. Raphael Hix, Eric J. Lentz, O. E. Bronson Messer, J. Austin Harris, Eirik Endeve, John M. Blondin, and Eric J. Lingerfelt, Phys. Rev. D **92**, 084040 (2015), arXiv:1505.05824 [astro-ph.HE].

[19] Takami Kuroda, Kei Kotake, and Tomoya Takiwaki, "A New Gravitational-wave Signature from Standing Accretion Shock Instability in Supernovae," Astrophys. J. Lett. **829**, L14 (2016), arXiv:1605.09215 [astro-ph.HE].

[20] H. Andresen, B. Müller, E. Müller, and H. Th. Janka, "Gravitational wave signals from 3D neutrino hydrodynamics simulations of core-collapse supernovae," MNRAS **468**, 2032–2051 (2017), arXiv:1607.05199 [astro-ph.HE].

[21] P. N. McDermott, H. M. van Horn, and J. F. Scholl, "Nonradial g-mode oscillations of warm neutron stars," ApJ **268**, 837–848 (1983).

[22] A. Reisenegger and P. Goldreich, "A new class of g-modes in neutron stars," ApJ **395**, 240–249 (1992).

[23] V. Ferrari, L. Gualtieri, J. A. Pons, and A. Stavridis, "Gravitational waves from rotating proto-neutron stars," Classical and Quantum Gravity **21**, S515–S519 (2004), astro-ph/0409578.

[24] A. Passamonti, M. Bruni, L. Gualtieri, and C. F. Sopuerta, "Coupling of radial and nonradial oscillations of relativistic stars: Gauge-invariant formalism," Phys. Rev. D **71**, 024022 (2005), gr-qc/0407108.

[25] H. Dimmelmeier, N. Stergioulas, and J. A. Font, "Nonlinear axisymmetric pulsations of rotating relativistic stars in the conformal flatness approximation," MNRAS **368**, 1609–1630 (2006), astro-ph/0511394.

[26] C. J. Krüger, W. C. G. Ho, and N. Andersson, "Seismology of adolescent neutron stars: Accounting for thermal effects and crust elasticity," Phys. Rev. D **92**, 063009 (2015), arXiv:1402.5656 [gr-qc].

[27] G. Camelio, A. Lovato, L. Gualtieri, O. Benhar, J. A. Pons, and V. Ferrari, "Evolution of a proto-neutron star with a nuclear many-body equation of state: neutrino luminosity and gravitational wave frequencies," ArXiv e-prints (2017), arXiv:1704.01923 [astro-ph.HE].

[28] H. Sotani and T. Takiwaki, "Gravitational wave asteroseismology with protoneutron stars," Phys. Rev. D **94**, 044043 (2016), arXiv:1608.01048 [astro-ph.HE].

[29] A. Torres-Forné, P. Cerdá-Durán, A. Passamonti, and J. A. Font, "Towards asteroseismology of core-collapse supernovae with gravitational-wave observations - I. Cowling approximation," MNRAS **474**, 5272–5286 (2018), arXiv:1708.01920 [astro-ph.SR].

[30] Viktoriya Morozova, David Radice, Adam Burrows, and David Vartanyan, "The Gravitational Wave Signal from Core-collapse Supernovae," ApJ **861**, 10 (2018), arXiv:1801.01914 [astro-ph.HE].

[31] A. Torres-Forné, P. Cerdá-Durán, A. Passamonti, M. Obergaulinger, and J. A. Font, "Towards asteroseismology of core-collapse supernovae with gravitational wave observations - II. Inclusion of spacetime perturbations," MNRAS **482**, 3967–3988 (2019), arXiv:1806.11366 [astro-ph.HE].

[32] A. Torres-Forné, P. Cerdá-Durán, M. Obergaulinger, B. Müller, and J. Font, "Universal relations for gravitational-wave asteroseismology of proto-neutron stars," Physical Review Letters **123**, 051102 (2019).

[33] Hajime Sotani, Takami Kuroda, Tomoya Takiwaki, and Kei Kotake, "Dependence of the outer boundary condition on protoneutron star asteroseismology with gravitational-wave signatures," Phys. Rev. D **99**, 123024 (2019), arXiv:1906.04354 [astro-ph.HE].

[34] John Ryan Westernacher-Schneider, Evan O'Connor, Erin O'Sullivan, Irene Tamborra, Meng-Ru Wu, Sean M. Couch, and Felix Malmenbeck, "Multimessenger asteroseismology of core-collapse supernovae," Phys. Rev. D **100**, 123009 (2019), arXiv:1907.01138 [astro-ph.HE].

[35] Hajime Sotani and Tomoya Takiwaki, "Dimension dependence of numerical simulations on gravitational waves from protoneutron stars," Phys. Rev. D **102**, 023028 (2020), arXiv:2004.09871 [astro-ph.HE].

[36] Hajime Sotani and Tomoya Takiwaki, "Avoided crossing in gravitational wave spectra from protoneutron star," MNRAS (2020), 10.1093/mnras/staa2597, arXiv:2008.00419 [astro-ph.HE].

[37] H. Dimmelmeier, J. A. Font, and E. Müller, "Relativistic simulations of rotational core collapse I. Methods, initial models, and code tests," A&A **388**, 917–935 (2002), arXiv:astro-ph/0204288 [astro-ph].

[38] Harald Dimmelmeier, Jérôme Novak, José A. Font, José M. Ibáñez, and Ewald Müller, "Combining spectral and shock-capturing methods: A new numerical

approach for 3D relativistic core collapse simulations," Phys. Rev. D **71**, 064023 (2005), arXiv:astro-ph/0407174 [astro-ph].

[39] B. Müller and H. Th. Janka, "Non-radial instabilities and progenitor asphericities in core-collapse supernovae," MNRAS **448**, 2141–2174 (2015), arXiv:1409.4783 [astro-ph.SR].

[40] O. Just, M. Obergaulinger, and H.-T. Janka, "A new multidimensional, energy-dependent two-moment transport code for neutrino-hydrodynamics," MNRAS **453**, 3386–3413 (2015), arXiv:1501.02999.

[41] A. Marek, H. Dimmelmeier, H.-T. Janka, E. Müller, and R. Buras, "Exploring the relativistic regime with Newtonian hydrodynamics: an improved effective gravitational potential for supernova simulations," A&A **445**, 273–289 (2006).

[42] S. E. Woosley, A. Heger, and T. A. Weaver, "The evolution and explosion of massive stars," Reviews of Modern Physics **74**, 1015–1071 (2002).

[43] S. E. Woosley and A. Heger, "Nucleosynthesis and remnants in massive stars of solar metallicity," Phys. Rep. **442**, 269–283 (2007), astro-ph/0702176.

[44] J. M. Lattimer and F. Douglas Swesty, "A generalized equation of state for hot, dense matter," Nuclear Physics A **535**, 331–376 (1991).

[45] A. W. Steiner, M. Hempel, and T. Fischer, "Core-collapse Supernova Equations of State Based on Neutron Star Observations," ApJ **774**, 17 (2013), arXiv:1207.2184 [astro-ph.SR].

[46] G. Shen, C. J. Horowitz, and S. Teige, "New equation of state for astrophysical simulations," Phys. Rev. C **83**, 035802 (2011), arXiv:1101.3715 [astro-ph.SR].

[47] .

[48] Lisa Barsotti, Peter Fritschel, Matthew Evans, and Slawomir Gras, "Updated advanced ligo sensitivity design curve," (2018).

[49] David Reitze, Rana X Adhikari, Stefan Ballmer, Barry Barish, Lisa Barsotti, GariLynn Billingsley, Duncan A. Brown, Yanbei Chen, Dennis Coyne, Robert Eisenstein, Matthew Evans, Peter Fritschel, Evan D. Hall, Albert Lazzarini, Geoffrey Lovelace, Jocelyn Read, B. S. Sathyaprakash, David Shoemaker, Joshua Smith, Calum Torrie, Salvatore Vitale, Rainer Weiss, Christopher Wipf, and Michael Zucker, "Cosmic explorer: The u.s. contribution to gravitational-wave astronomy beyond ligo," (2019), arXiv:1907.04833 [astro-ph.IM].

[50] S Hild, M Abernathy, F Acernese, P Amaro-Seoane, N Andersson, K Arun, F Barone, B Barr, M Barsuglia, M Beker, and et al., "Sensitivity studies for third-generation gravitational wave observatories," Classical and Quantum Gravity **28**, 094013 (2011).